LETTER

doi:10.1038/nature13526

Ramp compression of diamond to five terapascals

R. F. Smith[1], J. H. Eggert[1], R. Jeanloz[2], T. S. Duffy[3], D. G. Braun[1], J. R. Patterson[1], R. E. Rudd[1], J. Biener[1], A. E. Lazicki[1], A. V. Hamza[1], J. Wang[2], T. Braun[1], L. X. Benedict[1], P. M. Celliers[1] & G. W. Collins[1]

The recent discovery of more than a thousand planets outside our Solar System[1,2], together with the significant push to achieve inertially confined fusion in the laboratory[3], has prompted a renewed interest in how dense matter behaves at millions to billions of atmospheres of pressure. The theoretical description of such electron-degenerate matter has matured since the early quantum statistical model of Thomas and Fermi[4–10], and now suggests that new complexities can emerge at pressures where core electrons (not only valence electrons) influence the structure and bonding of matter[11]. Recent developments in shock-free dynamic (ramp) compression now allow laboratory access to this dense matter regime. Here we describe ramp-compression measurements for diamond, achieving 3.7-fold compression at a peak pressure of 5 terapascals (equivalent to 50 million atmospheres). These equation-of-state data can now be compared to first-principles density functional calculations[12] and theories long used to describe matter present in the interiors of giant planets, in stars, and in inertial-confinement fusion experiments. Our data also provide new constraints on mass–radius relationships for carbon-rich planets.

Mass–radius data for extrasolar planets combined with equation-of-state (EOS) models for constituent materials reveal that matter at pressures of several terapascals is quite common throughout the Universe[1,2,13]. At several terapascals, matter is approaching an atomic-scale pressure (for example, the quantum-mechanical 'pressure' that counteracts the electrons' Coulomb attraction in a Bohr atom), at which material structure and chemistry, and even the properties of atoms themselves, are expected to change[11]. Recent density functional theory (DFT) calculations predict that in several materials electrons become localized at terapascal conditions, with structural and electronic complexity unexpected from quantum statistical models (such as that of Thomas and Fermi)[12].

Experimental access to multi-terapascal conditions is now possible with dynamic ramped compression. Dynamic compression is necessary to achieve atomic-scale pressures, conditions far beyond those accessible in static experiments[14]. Ramp compression produces less dissipative heating, thus enabling higher compression and lower temperature than does shock compression[15]. However, ramp compression is unstable relative to a shock because sound velocities typically increase with pressure, so precise control of the applied pressure-loading history is required to achieve high pressures without shock formation.

The National Ignition Facility, a 2-MJ laser designed to create thermonuclear fusion in the laboratory[3], offers the energy and control necessary to ramp compress matter to several terapascals. Here we describe ramp-loading measurements on carbon to 5 TPa, with stress, density and sound speed determined for the entire compression path. These unprecedented conditions provide experimental constraints on the carbon EOS at pressures more than thirty times that of previous static-compression measurements, and where state-of-the-art DFT coincides with modern versions of the quantum-statistical Thomas–Fermi model, originally developed early in the past century to describe matter at extreme compressions.

In these experiments, 176 laser beams deliver a total peak power of 2.2 TW, with accuracy of better than 1% in power and 0.02 ns in time, over a duration of 20 ns. The light hitting a target (indirectly) creates an ablatively driven pressure wave in the sample (Fig. 1), and—because pressure scales as the 7/8th power of the laser intensity[16]—the pressure is controlled to better than 1%. Samples consist of nanocrystalline diamond, shaped with steps so that the pressure-wave transit across four different thicknesses is recorded for each experiment. Response of the sample is characterized by velocity interferometry (VISAR), which records the velocity of the sample's free (back) surface as it is engulfed by the pressure wave (Fig. 1). Iterative Lagrangian analysis is used to translate these velocity data into a stress–density relation that quantifies the loading path (Fig. 2)[17]. These data are absolute—not referenced against a

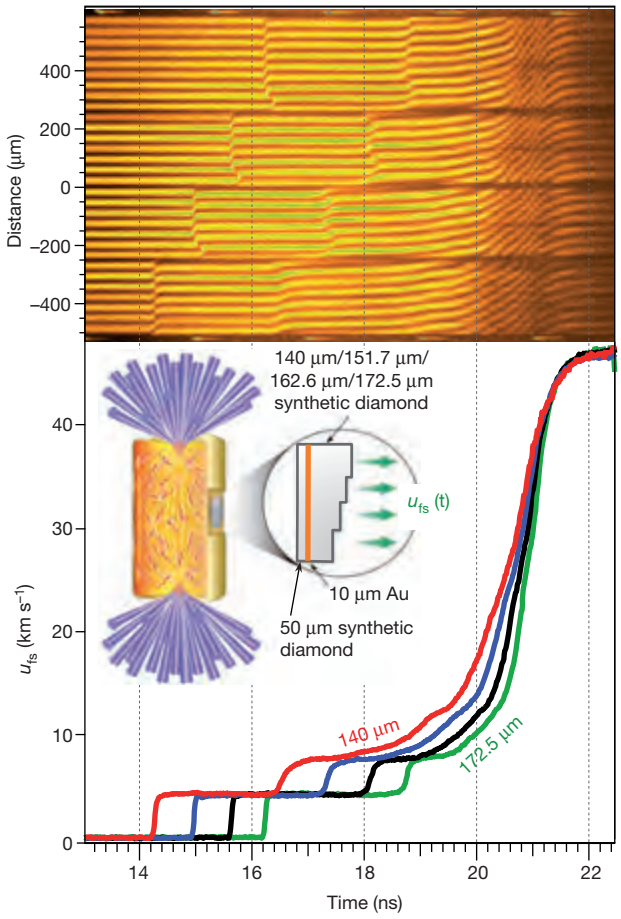

Figure 1 | Velocity interferometry for ramp compressed diamond. Top, the temporally resolved velocity interferometry record. Bottom, derived free-surface velocity u_{fs} versus time. The target (inset) consists of a gold cylinder (hohlraum) 6 mm in diameter by 11 mm long, inside which the 351-nm-wavelength laser light (purple beams) is converted to X-ray energy that is absorbed by the diamond sample attached to the side of the hohlraum. The X-rays ablate and ramp-compress the sample, and the free-surface velocity is recorded for four thicknesses of diamond: 140.0 μm (red line), 151.7 μm (blue line), 162.6 μm (black line) and 172.5 μm (green line) (see Methods).

[1]Lawrence Livermore National Laboratory, PO Box 808, Livermore, California 94550, USA. [2]Department of Earth and Planetary Science, Department of Astronomy and Miller Institute for Basic Research in Science, University of California, Berkeley, California 94720, USA. [3]Department of Geosciences, Princeton University, Princeton, New Jersey 08544, USA.

standard—which is important for quantifying the EOS and benchmarking condensed-matter theories in the terapascal regime.

In detail, we initiate loading with a shock wave of approximately 0.1 TPa, before the onset of the main ramp compression (Fig. 1). Such pre-ramp loading of diamond produces a more fluid-like (strength-free) state[18], which is important for reducing the dissipative heating that can limit compression. Longitudinal stress (P_x)—not pressure—is shown in Fig. 2, because our one-dimensional loading method creates a uniaxial strain that relaxes towards an isotropic state.

A typical record (Fig. 1) shows a free-surface velocity profile $u_{fs}(t)$, characterized by an initial shock to 4.1 km s^{-1}, followed by a fast rise and plateau at 7.2 km s^{-1}, and subsequent ramp compression to 46.6 km s^{-1} (3.7 TPa). Our analysis yields the Lagrangian sound speed (C_L) and P_x as functions of density ρ from the measured $u_{fs}(t)$ (Fig. 2)[17]. In all, three experiments yielded $C_L(\rho)$ and $P_x(\rho)$ to peak stresses of 2.7 TPa, 3.7 TPa and 5 TPa, respectively. C_L decreases abruptly at $u_{fs} = 4.1$ km s^{-1}, corresponding to a longitudinal stress of $P_{x,\,limit} = 0.11$ TPa, which we interpret to be the dynamic strength (elastic limit) of diamond. This also shows up as the slight deviation in the stress–density relation near 0.11 TPa (Fig. 2, inset). Hydrodynamic simulations indicate that the rapid rise and plateau in $u_{fs}(t)$ at 7.2 km s^{-1} corresponds to a reverberating compression wave within the intermediate Au layer (Fig. 1).

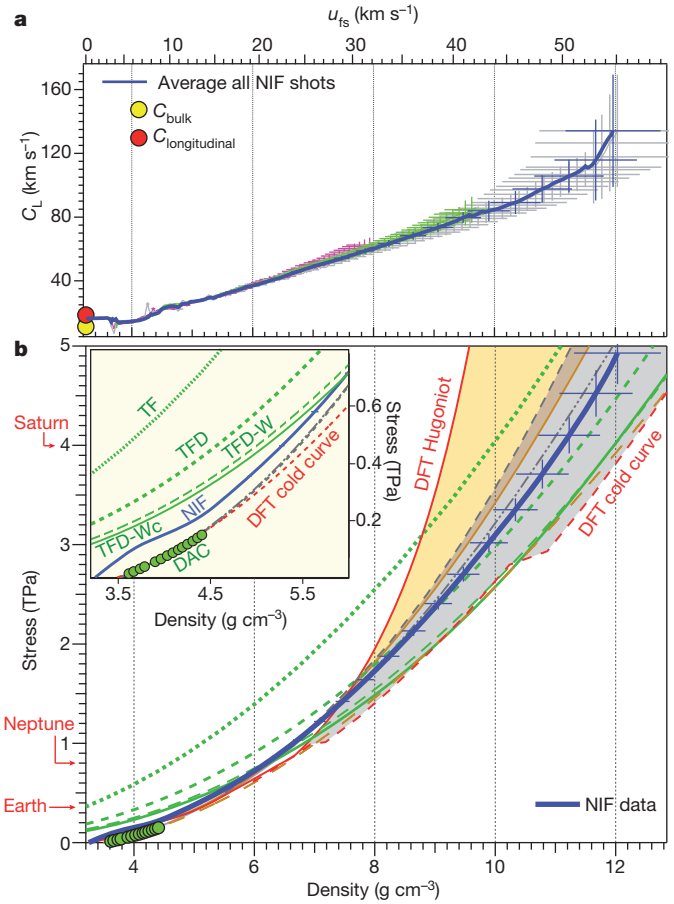

Figure 2 | Ramp compression stress and sound velocity measurements. **a**, Lagrangian sound velocity C_L versus density. **b**, Longitudinal stress P_x versus density. Three experiments (pink, light-green and grey lines) yield C_L data and their average (dark blue line), which are used to determine P_x–density[17] (dark blue line in **b**). Error bars, 1σ. Model comparisons include DFT (solid red line)[10] and Mie–Grüneisen (solid orange line) Hugoniots (density correction discussed in Methods); cold curves from DFT[12] (red dashed line), statistical-atom models (TF, TFD, TFD-W and TFD-Wc as green dotted, short dashed, long dashed and solid lines)[9], and Vinet[19] (grey dot-dashed line) and Birch–Murnaghan[20] (grey dashed line) EOS fits to static data[21,22]. Pressure-scale-corrected[21] static diamond anvil cell (DAC) data[22] are green circles. Shaded regions between cold curves (grey) or Hugoniots (orange) show roughly the range of uncertainty in the EOS in this terapascal regime. Central pressures for Earth, Neptune and Saturn are shown for reference. The inset highlights the differences in the models at low pressure.

These new data are compared to several carbon EOS models in the multi-terapascal regime (Fig. 2, Extended Data Fig. 1, Extended Data Table 1, and Methods). A cold curve derived from first-principles DFT[12] is in good agreement with a Mie–Grüneisen reduction and extrapolation of shock-Hugoniot data collected to 2 TPa. Also shown are the cold curve formulations from Vinet[19] and Birch–Murnaghan[20] each fitted to existing diamond anvil cell data[21,22]. (Even at these extreme pressures, the differences between the room-temperature isentrope and isotherm and the cold curve (0 K) are indistinguishable on this scale, so for consistency, we refer below simply to the cold curve.) For reference, the Hugoniots calculated from both DFT (solid red line) and a Mie–Grüneisen model (solid orange line) are shown in Fig. 2b. The DFT Hugoniot predicts carbon to be liquid and much less compressible than the DFT cold curve for stresses above about 1 TPa. The differences between the cold curves (grey band) and Hugoniots (orange band) in Fig. 2b illustrate the uncertainties in using prior data for extrapolating the carbon EOS into the terapascal regime.

The cold curve calculated by DFT shows a sequence of phase transformations: diamond to BC8 (body-centred cubic $Ia\bar{3}$) (at ~0.99 TPa), BC8 to simple cubic (at ~2.7 TPa)[12], which are apparent in stress–density curves as stress plateaus corresponding to increased densities (Fig. 2b). No such stress plateaus are apparent in our data. Although phase-transformation kinetics can smooth such features[23], determining whether or not these phase transformations occur will require further work[24]. Metadynamics calculations for carbon do indicate that the diamond-to-BC8 transition kinetics may be quite slow[25].

Static compression and elasticity measurements[21,22] up to their highest pressures (0.15 TPa) are indistinguishable from the DFT cold curve and standard EOS model fits to the data (Vinet and Birch–Murnaghan). However, when extrapolated to 5 TPa these models differ by about 20% in density (Fig. 2 and Fig. 3, inset). Our data lie between these cold curve calculations.

Also consistent with the DFT cold curve are the gradient-corrected (TFD-W) and the gradient-and-correlation-corrected (TFD-Wc) Thomas–Fermi–Dirac EOSs between about 2 TPa and 5 TPa (Fig. 2)[9]. This agreement is notable because the statistical-atom model considers neither crystal structure nor orbital information, whereas DFT includes both. This agreement may be partly fortuitous, because carbon might not yet be in its densest crystal structure at these pressures, and the deviation of statistical-atom theories is towards predicting densities that are systematically too low.

Our ramp data achieve higher density than the shock Hugoniot, consistent with temperatures being lower for ramp compression versus shock compression[15,26]. Moreover, these new data are somewhat less compressible than cold-isothermal compression calculations with DFT over most of the pressure range studied, and modern Thomas–Fermi–Dirac formulations (TFD-W and TFD-Wc). We expect that the overlap of the ramp compression data with the older uncorrected Thomas–Fermi–Dirac data in the 2–3 TPa regime is fortuitous. Sample temperature, material strength[18] and phase transformation kinetics[23] can each cause a less compressible stress–density path with respect to the cold curve, so these data should be considered an upper bound for such comparison. Indeed, further study is needed to obtain a better understanding of the differences between theory and experiment and to develop measurement techniques (such as for temperature and structural determination) with which to explore this new extreme matter regime.

The experimental techniques developed here provide a new capability to experimentally reproduce pressure–temperature conditions deep in planetary interiors. Carbon is the fourth most abundant element in the cosmos and has a potentially important role in many types of planets, both within and outside the Solar System. One proposed group of super-Earth exoplanets (1–10 Earth masses in size) are those enriched in carbon,

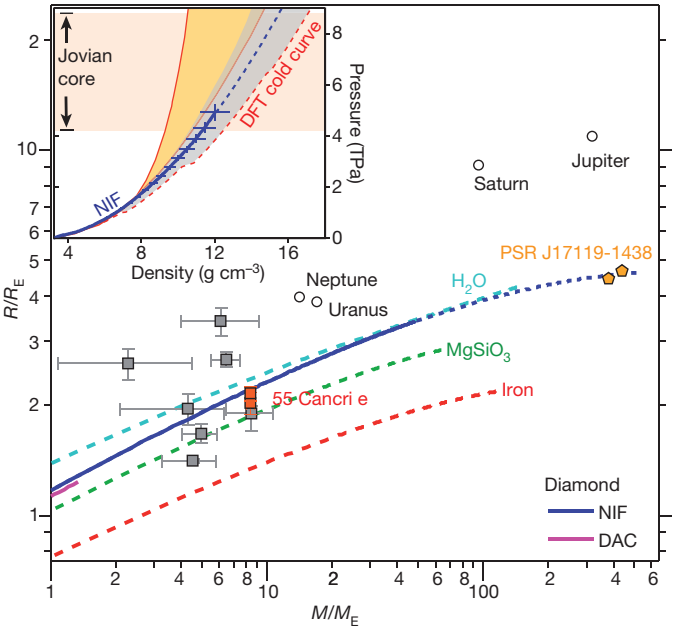

Figure 3 | Mass–radius relationships for homogenous-composition planets. Calculations for carbon (based on our data, where 1σ error bars are within the width of the line, dark blue), H_2O (light blue), post-perovskite $MgSiO_3$ (green) and iron (red)[13,30] (lines are dashed when based on extrapolated EOS data). Yellow symbols are values consistent with the minimum density for the companion object to pulsar PSR J1719-1438 for assumed orbital inclinations of 90 and 60 degrees[29]. The grey squares represent selected transiting super-Earths, with error bars as reported in ref. 27. Two possible values of radii R are shown for 55 Cancri e (red squares)[27]. The inset shows P_x–density relevant to Jupiter's core (~4.3–8.8 TPa)[28] with other curves as in Fig. 2. M_E and R_E are the mass and radius of the Earth, respectively.

and the planet 55 Cancri e has been proposed as a possible carbon planet[27]. Figure 3 shows mass–radius relationships for selected known super-Earths together with various hypothetical uniform-composition planets, including a pure-carbon planet based on our ramp-compression EOS. Using our new data, we find the central pressure for a 10-Earth-mass pure-carbon planet to be about 0.8 TPa. This new capability to reach multi-terapascal pressures also enables experimental access to Jupiter's core pressures[28] where extrapolations of earlier shock and static data become unreliable (Fig. 3, inset).

Our results also have relevance for large pulsar planets, such as the companion of millisecond pulsar PSR J1719-1438 (ref. 29). This object has a minimum mass somewhat larger than Jupiter (1.15×10^{-3} solar masses or 383 Earth masses), and a 2.2-hour orbital period. A carbon-rich composition was suggested, based on TFD-Wc results for carbon[9,29]. The reliability of this form of TFD theory as shown by our experiments supports this interpretation. An extrapolation of our EOS is consistent with TFD-Wc in suggesting that an object of this mass made of pure carbon would have a radius of about 4.5 Earth radii and a central pressure of about 148 TPa. The mean density of 23 g cm^{-3} is compatible with the measured minimum density of the pulsar planet[29].

In summary, diamond, the least compressible material known, has here been compressed to an unprecedented density of 12 g cm^{-3}, more than that of lead at ambient conditions. The measured Lagrangian sound speed, stress and density provide the first experimental data for constraining condensed-matter theory and planet-evolution models in the terapascal regime. By realizing three necessary conditions—(1) the adiabatic conditions of dynamic compression; (2) a loading profile soft enough to avoid shock formation; and (3) a nearly fluid-like response of the sample such that strength and dissipation are minimal—these experiments document an approach for taking solids to the long-sought high-density conditions of statistical-electron theory.

METHODS SUMMARY

Experiments used 176 laser beams from the National Ignition Facility (NIF) (in Livermore, California, USA) focused onto the inner walls of a gold hohlraum (a gold cylinder that converts the laser light to X-rays) with a combined laser energy up to 0.76 MJ in a ~20-ns temporally ramped pulse. This generates a spatially uniform near-blackbody distribution of thermal X-rays in the hohlraum with a characteristic radiation temperature T_r, which increases with time to a peak of $T_r \approx 235$ eV. The subsequent X-ray ablation of the diamond, over a 3-mm diameter, produces a uniform ramp-compression wave, which outruns the thermal wave produced by ablation. As the pressure wave reaches the back surface of the diamond the free surface velocity of each step is recorded with an imaging velocity interferometer (Fig. 1).

Samples consist of a 50-μm-thick diamond plate used as an ablator, a 10-μm Au layer preheat shield, and a diamond sample having four steps (Fig. 1 inset). The diamond was synthesized by chemical vapour deposition to yield a layered microstructure with an average grain size of 200 nm and a density of 3.2491 g cm^{-3} ($\pm$0.01%). The final sample had alternating 0.35-μm layers of 20-nm grains and ~350-nm grains. X-ray diffraction showed a <110> texture in the growth direction. The thickness of the composite sample is determined to $\pm$1.0 μm, and the differences in step thickness are determined by optical interferometry to $\pm$0.1 μm. The Au layer was incorporated into the target design to serve as a radiation preheat shield for the step diamond sample. Detailed radiation transport simulations estimate a temperature rise of 33 K due to X-ray preheating.

Online Content Methods, along with any additional Extended Data display items and Source Data, are available in the online version of the paper; references unique to these sections appear only in the online paper.

Received 8 October 2013; accepted 16 May 2014.

1. Schneider, J., Dedieu, C., Le Sidaner, P., Savalle, R. & Zolotukhin, I. Defining and cataloging exoplanets: the exoplanet.eu database. *Astron. Astrophys.* **532,** A79 (2011).
2. Seager, S., Kuchner, M., Hier-Majumder, C. A. & Militzer, B. Mass-radius relationships for solid exoplanets. *Astrophys. J.* **669,** 1279–1297 (2007).
3. Edwards, M. J. *et al.* Progress towards ignition on the National Ignition Facility. *Phys. Plasmas* **20,** 070501 (2013).
4. Thomas, L. H. The calculation of atomic fields. *Math. Proc. Camb. Phil. Soc.* **23,** 542–548 (1927).
5. Dirac, P. A. M. Note on exchange phenomena in the Thomas atom. *Math. Proc. Camb. Phil. Soc.* **26,** 376–385 (1930).
6. Feynman, R. P., Metropolis, N. & Teller, E. Equation of state of elements based on the generalized Fermi-Thomas theory. *Phys. Rev.* **75,** 1561–1573 (1949).
7. Salpeter, E. E. & Zapolsky, H. S. Theoretical high pressure equations of state, including correlation energy. *Phys. Rev.* **158,** 876–886 (1967).
8. Abrahams, A. M. & Shapiro, S. L. Cold equation of state from Thomas-Fermi-Dirac-Weizsacker theory. *Phys. Rev. A* **42,** 2530–2538 (1990).
9. Lai, D., Abrahams, A. M. & Shapiro, S. L. Equation of state in metals and cold stars: evaluation of statistical models. *Astrophys. J.* **377,** 612–628 (1991).
10. Correa, A. A., Benedict, L. X., Young, D. A., Schwegler, E. & Bonev, S. A. A first principles multi-phase equation of state of carbon under extreme conditions. *Phys. Rev. B* **78,** 024101 (2008).
11. Neaton, J. B. & Ashcroft, N. W. Pairing in dense lithium. *Nature* **400,** 141–144 (1999).
12. Martinez-Canales, M., Pickard, C. J. & Needs, R. J. Theormodynamically stable phase of carbon at multiterapascal pressures. *Phys. Rev. Lett.* **108,** 045704 (2012).
13. Swift, D. C. *et al.* Mass-radius relationships for exoplanets. *Astrophys. J.* **744,** 59–68 (2012).
14. Dubrovinsky, L., Dubrovinskaia, N., Prakapenka, V. B. & Abakumov, A. M. Implementation of micro-ball nanodiamond anvils for high-pressure studies above 6 Mbar. *Nature Commun.* **3,** 1163 (2012).
15. Zel'dovich, Ya. B. & Raizer, Yu. P. *Physics of Shock Waves and High-Temperature Hydrodynamic Phenomena* (Dover, 2002).
16. Atzeni, S. & Meyer-ter-Vehn, J. *The Physics of Inertial Fusion: Beam Plasma Interaction, Hydrodynamics, Hot Dense Matter* (Oxford Univ. Press, 2004).
17. Rothman, S. D. *et al.* Measurement of the principle isentropes of lead and lead-antimony alloy to ~400 kbar by quasi-isentropic compression. *J. Phys. D* **38,** 733–740 (2005).
18. McWilliams, R. S. *et al.* Strength effects in diamond under shock compression from 0.1 to 1 TPa. *Phys. Rev. B* **81,** 014111 (2010).
19. Vinet, P., Ferrante, J., Rose, J. H. & Smith, J. R. Compressibility of solids. *J. Geophys. Res.* **92,** 9319–9325 (1987).
20. Birch, F. Finite elastic strain of cubic crystals. *Phys. Rev.* **71,** 809–824 (1947).
21. Dewaele, A., Datchi, F., Loubeyre, P. & Mezouar, M. High pressure-high temperature equation of state of neon and diamond. *Phys. Rev. B* **77,** 094106 (2008).
22. Occelli, F., Loubeyre, P. & Letoullec, R. Properties of diamond under hydrostatic pressures up to 140 GPa. *Nature Mater.* **2,** 151–154 (2003).
23. Smith, R. F. *et al.* Time-dependence of the alpha to epsilon phase transformation in iron. *J. Appl. Phys.* **114,** 223507 (2013).
24. Coppari, F. *et al.* Experimental evidence for a phase transition in magnesium oxide at exoplanet pressures. *Nature Geosci.* **6,** 926–929 (2013).

25. Sun, J., Klug, D. D. & Martoňák, R. Structural transformations in carbon under extreme pressure: beyond diamond. *J. Chem. Phys.* **130,** 194512 (2009).
26. Eggert, J. H. *et al.* Melting temperature of diamond at ultrahigh pressure. *Nature Phys.* **6,** 40–43 (2010).
27. Madhusudhan, N., Lee, K. K. M. & Mousis, O. A possible carbon-rich interior in super-Earth 55 Cancri e. *Astrophys. J.* **759,** L40 (2012).
28. Nettelmann, N. *et al.* Ab initio equation of state data for hydrogen, helium, and water and the internal structure of Jupiter. *Astrophys. J.* **683,** 1217–1228 (2008).
29. Bailes, M. *et al.* Transformation of a star into a planet in the millisecond Pulsar binary. *Science* **333,** 1717–1720 (2011).
30. Wagner, F. W., Sohl, F., Hussmann, H., Grott, M. & Rauer, H. Interior structure models of solid exoplanets using material laws in the infinite pressure limit. *Icarus* **214,** 366–376 (2011).

Acknowledgements We thank the NIF staff, B. Goldstein, Ed Moses, C. Keane, the Science Use of NIF programme, C. Wild (Fraunhofer Institute for Applied Solid-State Physics, Freiburg, Germany) for preparation of the diamond targets, D. Hicks for his analysis work, and M. Millot for reanalysing published diamond Hugoniot data. This work was performed under the auspices of the US Department of Energy by Lawrence Livermore National Laboratory under contract number DE-AC52-07NA27344, with additional support from the Department of Energy, the University of California, and the Miller Institute for Basic Research in Science.

Author Contributions R.F.S., J.H.E., D.G.B., P.M.C., J.R.P., A.E.L. and G.W.C. designed, executed and analysed the data from the ramp compression experiments. J.H.E., R.E.R., L.X.B., R.J., T.S.D., J.W. and G.W.C. performed the comparisons of experimental data to EOS models and theory. J.B., T.B. and A.V.H. were instrumental in procuring and metrologizing the diamond step samples.

Author Information Reprints and permissions information is available at www.nature.com/reprints. The authors declare no competing financial interests. Readers are welcome to comment on the online version of the paper. Correspondence and requests for materials should be addressed to G.W.C. (collins7@llnl.gov).

METHODS

Ramp-compression design to terapascal pressures. The inner wall of a gold hohlraum (a gold cylinder used to convert laser light to X-rays) was illuminated with 176 beams of the NIF with a combined energy up to 0.76 MJ in a ~20-ns temporally ramped pulse. This generates a near-blackbody distribution of thermal X-rays with a characteristic radiation temperature T_r, which increases with time to a peak of $T_r \approx 235$ eV. The hohlraum was filled with 0.1 atmosphere of neopentayne (C_5H_{12}) gas, which enabled the hohlraum cavity to stay open so that input laser power could be coupled effectively at late times. The C_5H_{12} gas was held within the hohlraum by 0.6-μm-thick polyimide windows covering the laser entrance holes. The X-ray ablation of diamond produces a uniform ramp-compression wave that transits the diamond sample. As the compression wave reaches the back of the sample, the surface accelerates into free space, and the free-surface velocity history u_{fs} for each step is recorded with a line-imaging velocity interferometer (VISAR) (Fig. 1). Our laser pulse shape is designed to launch an initial elastic shock into the diamond sample in advance of the ramp-compression wave. This shock feature—observed in the free-surface velocity record at $u_{fs} = 4.1$ km s^{-1} (Fig. 1) and corresponding to $P_{x,\mathrm{limit}} = 0.11$ TPa—is interpreted as the dynamic strength (elastic limit) of diamond. The corresponding dynamic yield strength Y_0 is determined from $Y_0 = P_{x,\mathrm{limit}}(1-2\nu)/(1-\nu)$, with the Poisson's ratio, $\nu = 0.18$, derived from our sound-speed data (Fig. 2a) from $\left(\frac{C_{\mathrm{longitudinal}}}{C_{\mathrm{bulk}}}\right)^2 = 3\left(\frac{1-\nu}{1+\nu}\right)$. This yields $Y_0 = 0.085$ TPa, which is less than observed in static experiments[31] ($Y_0 = 0.13$–0.15 TPa) but consistent with the values 0.069 TPa$< Y_0 <$ 0.096 TPa reported for ramp compression of diamond with micrometre grain size[32]. The presence of an initial shock results in a loss of diamond strength[18], with expected lower levels of compressive work heating over pure ramp compression[32] and, therefore, a lower-temperature compression path.

Target design. Our samples consist of a 50-μm-thick diamond plate used as an ablator, a 10-μm-thick Au layer preheat shield, and a diamond plate having four steps (Fig. 1, inset). The diamond was synthesized by chemical vapour deposition to yield a layered microstructure with an average grain size of 200 nm and a density of 3.2491 g cm^{-3} (±0.01%)[33,34]. The final sample had alternating 0.35-μm-thick layers of 20-nm grains and ~350-nm grains. X-ray diffraction showed a <110> texture in the growth direction. The thickness of the sample is determined to ±1.0 μm, including uncertainties in the diamond ablator and Au thicknesses, whereas the differences in step thickness are determined by optical interferometry to ±0.1 μm. The diamond sample was then attached to the Au with a ~3-μm-thick glue layer. The Au layer was incorporated into the target design to serve as a radiation preheat shield. Detailed radiation transport simulations estimate a temperature rise of 33 K, due to X-ray preheating.

Velocity interferometry. The response of the sample is characterized by velocity interferometry (VISAR), which records the velocity of the sample's free (back) surface as it is engulfed by the pressure wave (Fig. 1). The VISAR (Velocity Interferometer System for Any Reflector) diagnostic uses a line-focused 660-nm-wavelength laser beam to monitor a ~1-mm strip across all four steps of the sample[35]. Changes in velocity of the diamond free surface produce phase shifts in interference fringes that are recorded with a streak camera (Fig. 1). A typical VISAR record has a 30-μm spatial resolution, a 10-ns streak window with 0.01-ns resolution, and a velocity resolution of 0.1 km s^{-1}.

Stress–density analysis. Iterative Lagrangian analysis is used to translate these velocity data into a stress–density relation that quantifies the loading path (Fig. 2)[17,36]. The Lagrangian analysis method developed by Aidun and Gupta[36] and modified by Rothman[17] was used to determine the Lagrangian sound speed $C_L(u)$ and the stress–density ($P_x - \rho$) relation from the measured $u_{fs}(t)$ data, where u is the particle speed, and u_{fs} is the sample's free surface velocity (across each of four thicknesses). Metrology of the sample surface showed that the roughness was <0.1 μm, thickness gradients were <1%, and step heights were accurate to within 0.1 μm. In all, three shots gave $C_L(u)$ and $P_x - \rho$ data. $C_L(u)$ and its uncertainty $\sigma_{C_L}(u)$ are obtained from thickness and velocity-versus-time data by linear regression using errors determined by our measurement accuracies: u_{fs} (0.05 km s^{-1}), time (10 ps), and step height (100 nm). The uncertainty is propagated by calculating the weighted mean average of all three shots, $C_L(u) = \sum_j \frac{C_{L,j}}{\sigma^2_{C_{L,j}}} \Big/ \sum_j \frac{1}{\sigma^2_{C_{L,j}}}\Big|_u$, as shown by the blue curve in Fig. 2a, where j is the shot number. The uncertainty in the average value is chosen from the maximum of the uncertainty in the mean and the weighted standard deviation. $C_L(u)$ and σ_{C_L} are integrated to obtain $P_x = \rho_0 \int_0^u C_L\,\mathrm{d}u$, $\rho = \rho_0\left(1 - \int_0^u \frac{\mathrm{d}u}{C_L}\right)^{-1}$, and their uncertainties $\sigma_{P_x} = \rho_0 \int_0^u \sigma_{C_L}\,\mathrm{d}u$ and $\sigma_\rho = \frac{\rho^2}{\rho_0}\int_0^u \frac{\sigma_{C_L}}{C_L^2}\,\mathrm{d}u$. Uncertainties are propagated though the integrals linearly, rather than in quadrature, because σ_{C_L} appears to be strongly correlated rather than random. This method of uncertainty propagation allows the direct propagation of experimental uncertainties to $P_x - \rho$. Sound speed analysis over the three steps (four thicknesses) show simple wave behaviour, suggesting that the material response is not time-dependent within the experimental uncertainties.

Release waves from the diamond-vacuum interface significantly perturb the incoming ramp wave. Extensive tests using simulated data confirm that the iterative Lagrangian analysis accurately corrects for these wave interactions.

Mie–Grüneisen Hugoniot and cold curve. We compare our stress–density data (Fig. 2b and Extended Data Fig. 1) to a Hugoniot and cold curve reduced from available diamond Hugoniot data. There are several ways to construct a Mie–Grüneisen EOS, and here we begin with the relation for the pressure relative to a reference pressure P_{ref}

$$P(\eta,E) = P_{\mathrm{ref}}(\eta) + \rho_0\eta\gamma(E - E_{\mathrm{ref}}(\eta)) \tag{1}$$

where $\eta = \frac{\rho}{\rho_0}$ is the compression, γ is the Grüneisen parameter (assumed to depend only on density) and ρ_0 is the initial density. We can use either the Hugoniot or isotherm data to determine the reference states. Here we use the diamond Hugoniot data as the reference using a linear fit to existing shock velocity versus particle velocity data[18,37–40]

$$Us = C + sUp \tag{2}$$

where $C = 12.0$ km s^{-1} and $s = 1.04$. From this we obtain

$$P_{\mathrm{ref}}(\eta) = P_{\mathrm{H}}(\eta) = \rho_0\eta\frac{C^2(\eta-1)}{(\eta - s(\eta-1))^2} \tag{3}$$

$$E_{\mathrm{ref}}(\eta) = E_{\mathrm{H}}(\eta) = \frac{C^2(\eta-1)^2}{2(\eta - s(\eta-1))^2} \tag{4}$$

where $P_{\mathrm{H}}(\eta)$ and $E_{\mathrm{H}}(\eta)$ are the Hugoniot pressure and energy, respectively. Finally, from equation (1) we obtain the cold curve

$$P_0(\eta) = \rho_0\eta\left(\frac{C^2(\eta-1)}{(\eta - s(\eta-1))^2} + \gamma\left(E_0 - \frac{C^2(\eta-1)^2}{2(\eta - s(\eta-1))^2}\right)\right) \tag{5}$$

where we solve for $E_0(\eta)$ by

$$\begin{aligned}\frac{\mathrm{d}E_0}{\mathrm{d}\eta} &= \frac{1}{\rho_0\eta^2}\left(P_{\mathrm{H}} + \rho_0\gamma\eta(E_0 - E_{\mathrm{H}})\right)\\ &= \frac{1}{\eta}\left(\frac{C^2(\eta-1)}{(\eta - s(\eta-1))^2} + \gamma\left(E_0 - \frac{C^2(\eta-1)^2}{2(\eta - s(\eta-1))^2}\right)\right)\end{aligned} \tag{6}$$

It is also assumed $\gamma = \gamma_0\eta^{-q}$, where $\gamma_0 = 0.85$ (ref. 21). The variable q has not been measured at high pressure, and can have a significant impact on the cold curve determined. We find that a value of $q = 1$ yields a cold curve centred on the DFT-calculated cold curve[12]. This value of q is consistent with static measurements at pressures <0.1 TPa (ref. 21). This simple model for calculating the cold curve does not incorporate volume changes from proposed high-pressure phase transformations.

Calculation of 7.6% porous Hugoniot. The calculation is as shown in Fig. 2 and Extended Data Fig. 1**.** Our samples had a measured ambient density of 3.249 g cm^{-3} which is 7.6% below full crystal density. To calculate the stress-density path of a 7.6% porous Hugoniot we use the expression of McQueen[41]

$$P_x^*(\rho) = P_{\mathrm{H}}\frac{1 - (\gamma/2)\left(\frac{\rho}{\rho_0} - 1\right)}{1 - (\gamma/2)\left(\frac{\rho}{\rho_0^*} - 1\right)} \tag{7}$$

where $P_x^*(\rho)$ is the stress state along the porous Hugoniot at a density ρ, ρ_0 is the initial full crystal density (3.515 g cm^{-3}), ρ_0^* is the initial porous density (3.249 g cm^{-3}) and $\gamma(\rho)$ is the Grüneisen parameter. We note that implicit within the porous Hugoniot expression in equation (7) is that the wave is steady and the pores have collapsed completely in the post-shock state, that is, $P_x^*(\rho) = 0$ for $\rho_0^* \to \rho_0$; an assumption which is incorrect for diamond. Equation (7) is therefore a poor estimate for weak shocks but in cases where the shock pressure greatly exceeds the material strength (after the pores have closed) it is reasonable.

Upon compression, the material strength determines how much stress is needed to reduce the porosity to a given level. This relationship can be summarized in a crush-up curve: $\rho = \rho(\rho_0^*, P_x^*, E)$[42–44]. Following Carroll and Holt[43], pore crush-up is only initiated after a critical longitudinal stress, $P_{\mathrm{crit}} = \frac{2}{3}Y_0|\ln f_0|$ where Y_0 is the yield strength and f_0 is the initial porosity. For our diamond samples $Y_0 = 0.085$ TPa, $f_0 = \rho_0^*/\rho_0 = 0.076$ and $P_{\mathrm{crit}} = 0.146$ TPa. For $0 \le P \le P_{\mathrm{crit}}$, the pressure-dependent

pore fraction $f = f_0$ and the material is assumed to deform elastically. For $P > P_{crit}$, the porosity decays exponentially as $f = e^{-3P_x/2Y_0}$.

A number of studies on shock compression of under-dense materials have shown that rapid heating due to pore closure and the resultant increase in thermal pressure gives rise to reduced compression[41]. In Extended Data Fig. 1 this is witnessed by the stiffer response of the calculated porous Hugoniot compared to the Hugoniot for full-density diamond.

Diamond EOS data and DFT calculations. Extended Data Fig. 1 compares our data (initial density $\rho_0 \approx 3.249\ g\,cm^{-3}$) with previously reported shock Hugoniot[18,37–40], static[22], and ramp compression[32] data ($\rho_0 \approx 3.515\ g\,cm^{-3}$) as stress versus density. Shock Hugoniot data rely on knowledge of a reference material and therefore subsequent revisions of the reference EOS can change the reported diamond Hugoniot data. The Hugoniot points shown in Extended Data Fig. 1 have been reanalysed to account for new standard EOS as follows: The data reported by Nagao[38] and four of the high pressure points of Hicks[40] (open pentagons) used aluminium as a standard and were reanalysed using impedance matching[45] with the latest fit to the aluminium Hugoniot[46]. The highest pressure point of Hicks used a Mo standard and remains unchanged. Additional data reported by Hicks[40] and data reported by Brygoo[39] used a quartz standard. These data have been reanalysed using the constant Grüneisen re-shock model in ref. 40 and the quartz Hugoniot used as a reference is a fit of all available data for quartz shocked into the liquid phase[46,47].

The DFT EOS we use to produce the Hugoniot in Fig. 2 and Extended Data Fig. 1 is as reported[10], except without the embedding into the Thomas–Fermi-based quotidian-EOS (QEOS) model. We omit the connection with the QEOS model because the transition region between *ab initio* and QEOS models in ref. 10 created unphysical kinks in the EOS and resulting Hugoniot. The extrapolation of the more limited-range *ab initio* EOS of ref. 10 to the conditions relevant for the Hugoniot final states shown in our figures is expected to be quite accurate[48]. The DFT cold curve generated from ref. 10 is in good agreement with the DFT cold curve reported in ref. 12 (red dashed curve in Fig. 2 and Extended Data Fig. 1) for stresses less than 2.5 TPa (which is the pressure below which *ab initio* electronic structure information was used to construct that EOS).

Static-compression and elasticity measurements to 0.15 TPa are indistinguishable from the cold curves presented here[21,22]. The fit to the static compression measurements over this low compression range ($\rho/\rho_0 \approx 1.18$) are insensitive to the form of EOS used to fit the data (for example, Vinet[19], Birch–Murnaghan[20], or Holzapfel[49]). The Vinet EOS plotted in Fig. 2 and Extended Data Fig. 1 use $K_0 = 445$ GPa and $K'_0 = 4.18$ as reported in ref. 21. The values used for the Birch–Murnaghan ($K_0 = 445$ GPa, $K'_0 = 3.90(0.04)$) and Holzapfel ($K_0 = 445$ GPa, $K'_0 = 3.95(0.05)$) forms of EOS are based on fits to previous isothermal data[21,22]. Here the values from ref. 22 have been reanalysed using the revised ruby pressure scale as reported in ref. 21. Extrapolating these isothermal data to the multi-terapascal regime becomes highly uncertain depending on the EOS used (Fig. 2b and Extended Data Fig. 1).

Although temperature was not measured in these experiments, it is useful to comment on such estimates from theoretical calculations. The temperature calculated from DFT along the diamond principal isentrope is quite low even at the most extreme compressions studied here (~600 K to 700 K at multi-terapascal pressures). For this reason, the principal isentrope and the room-temperature isotherm are predicted to be nearly coincident in stress–density space. It is certainly possible that our ramp compression path have higher temperatures than these isentrope predictions and this may be responsible for the higher stress versus density. However, because temperature, material strength[18], and phase transformation kinetics[23] can each cause a stiffer response with respect to the isentrope, current estimates for the ramp compression temperature into the terapascal regime are quite speculative.

31. Eremets, M. I. *et al.* The strength of diamond. *Appl. Phys. Lett.* **87,** 141902 (2005).
32. Bradley, D. K. *et al.* Diamond at 800 GPa. *Phys. Rev. Lett.* **102,** 075503 (2009).
33. Reichart, P. *et al.* Three-dimensional hydrogen microscopy in diamond. *Science* **306,** 1537–1540 (2004).
34. Dawedeit, C. *et al.* Grain size dependent physical and chemical properties of thick CVD diamond films for high energy density physics experiments. *Diamond Rel. Mater.* **40,** 75–81 (2013).
35. Celliers, P. M. *et al.* Line-imaging velocimeter for shock diagnostics at the Omega laser facility. *Rev. Sci. Instrum.* **75,** 4916–4929 (2004).
36. Aidun, J. B. & Gupta, Y. M. Analysis of Lagrangian gauge measurements of simple and nonsimple plane waves. *J. Appl. Phys.* **69,** 6998–7014 (1991).
37. Knudson, M. D., Desjarlais, M. P. & Dolan, D. H. Shock-wave exploration of the high-pressure phases of carbon. *Science* **322,** 1822–1825 (2008).
38. Nagao, H. *et al.* Hugoniot measurement of diamond under laser shock compression up to 2 TPa. *Phys. Plasmas* **13,** 052705 (2006).
39. Brygoo, S. *et al.* Laser-shock compression of diamond and evidence of a negative-slope melting curve. *Nature Mater.* **6,** 274–277 (2007).
40. Hicks, D. G. *et al.* High-precision measurements of the diamond Hugoniot in and above the melt region. *Phys. Rev. B* **78,** 174102 (2008).
41. McQueen, R. G., Marsh, S. P., Taylor, J. W., Fritz, J. N. & Carter, W. J. in *High Velocity Impact Phenomena* Ch. 7, 293–417 (Academic Press, 1970).
42. Herrmann, W. Constitutive equation for the dynamic compaction of ductile porous materials. *J. Appl. Phys.* **40,** 2490–2499 (1969).
43. Carroll, M. M. & Holt, A. C. Static and dynamic pore-collapse relations for ductile porous materials. *J. Appl. Phys.* **43,** 1626–1636 (1972).
44. Reisman, D. B., Wolfer, W. G., Elsholz, A. & Furnish, M. D. Isentropic compression of irradiated stainless steel on the Z accelerator. *J. Appl. Phys.* **93,** 8952–8957 (2003).
45. Celliers, P. M. *et al.* Systematic uncertainties in shock-wave impedance-match analysis and the high-pressure equation of state of Al. *J. Appl. Phys.* **98,** 113529 (2005).
46. Knudson, M. D. & Desjarlais, M. P. Adiabatic release measurements in α-quartz between 300 and 1200 GPa: characterization of α-quartz as a shock standard in the multimegabar regime. *Phys. Rev. B* **88,** 184107 (2013).
47. Hicks, D. G. *et al.* Shock compression of quartz in the high-pressure fluid regime. *Phys. Plasmas* **12,** 082702 (2005).
48. Benedict, L. X. *et al.* A multiphase equation of state for carbon addressing high pressures and temperatures. Preprint at http://arxiv.org/abs/1311.4577 (2013).
49. Holzapfel, W. Equations of state for ideal and real solids under strong compression. *Europhys. Lett.* **16,** 67 (1991).

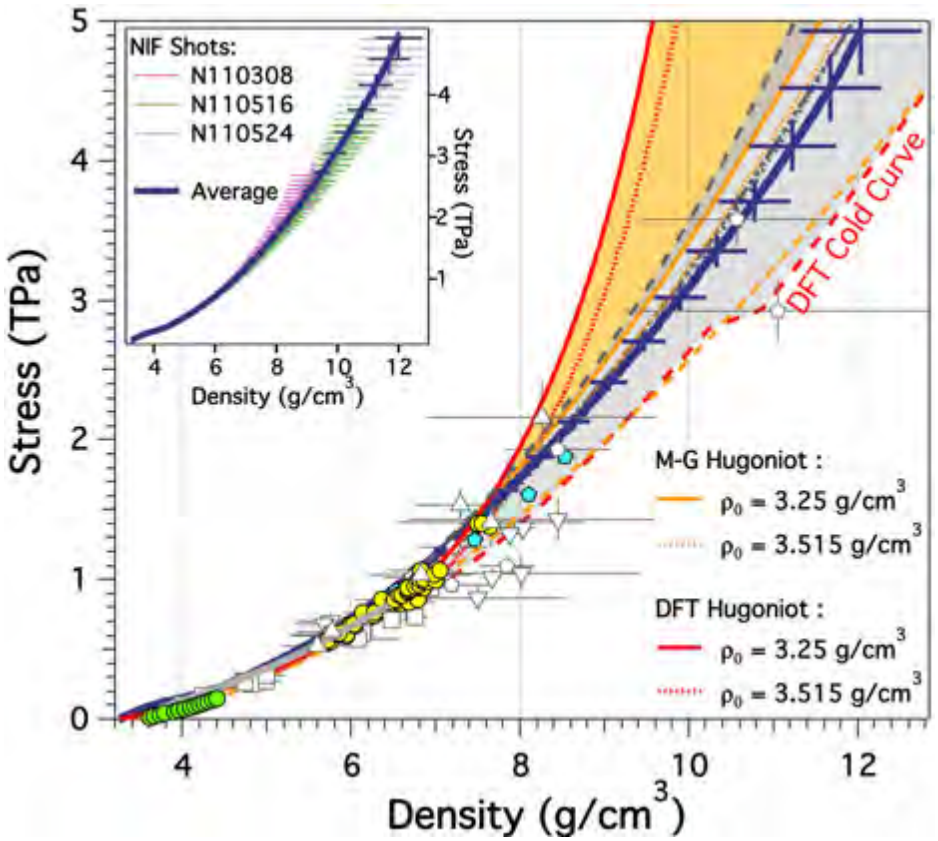

Extended Data Figure 1 | Ramp-compressed diamond stress versus density compared to other high-pressure data. NIF ramp-compression data with 1σ error bars (solid blue line) together with calculated Hugoniots (low-initial-density diamond, solid red line; standard-initial-density diamond, dotted red line) and the calculated cold curve (dashed red line)[12] from DFT; a simple Mie–Grüneisen model reduction of Hugoniot data to produce an extrapolated Hugoniot (low-initial-density diamond, solid orange line; standard-initial-density diamond, dotted orange line), and cold curve (dashed orange line); Vinet[19] (dot-dashed grey line), Birch-Murnaghan[20] (dashed grey line), and Holzapfel[49] (dotted grey line) extrapolations of 300-K diamond anvil cell data[21,22]. The shaded regions show the range of different models for cold curve (grey) and Hugoniot (orange) showing roughly the range of uncertainty in this ultrahigh-pressure regime. Also shown are data from shock experiments (yellow circles[37], up triangles[38], open pentagons (which used an Al or Mo standard)[40], down triangles[39], blue pentagons (which used the more accurate quartz standard)[40], open squares[18]), isothermal static data (green circles are ruby-corrected data[21,22]) and the ramp-compression data of Bradley[32] (solid grey line). The ramp-compression data of Bradley used full-density diamond and did not use an initial shock as in NIF data. The inset shows the calculated stress–density relations of the three NIF shots: N110308, N110516 and N110524, showing the level of repeatability between experiments.

Extended Data Table 1 | Ramp-compressed diamond stress–density data

P_x (GPa)	σ_{P_x} (GPa)	ρ (g/cm^3)	σ_ρ (g/cm^3)	P_x (GPa)	σ_{P_x} (GPa)	ρ (g/cm^3)	σ_ρ (g/cm^3)
0	0	3.25	0	1422	25	7.47	0.13
39.2	0.3	3.4	0	1487	27	7.58	0.14
79	0.7	3.57	0	1554	29	7.7	0.14
98.8	0.8	3.66	0	1623	31	7.82	0.15
117	1	3.76	0.01	1694	33	7.94	0.16
133.8	1.1	3.88	0.01	1766	35	8.06	0.17
151	1.3	4	0.01	1839	38	8.18	0.18
168.7	1.4	4.13	0.01	1915	40	8.31	0.19
187.8	1.6	4.25	0.01	1992	43	8.43	0.2
210	1.9	4.37	0.01	2071	46	8.55	0.21
234	2.1	4.48	0.02	2152	49	8.68	0.22
261	2.4	4.58	0.02	2235	52	8.8	0.23
289	2.8	4.69	0.02	2320	55	8.93	0.24
318	3.2	4.79	0.02	2406	59	9.05	0.25
348	3.6	4.9	0.02	2495	62	9.18	0.27
379	4	5	0.03	2585	66	9.31	0.28
412	4.5	5.11	0.03	2678	70	9.44	0.29
445	5	5.22	0.03	2774	74	9.57	0.3
480	5.5	5.33	0.04	2871	79	9.7	0.32
516	6	5.44	0.04	2969	85	9.83	0.34
553	6.6	5.55	0.04	3069	92	9.96	0.36
592	7.3	5.66	0.05	3170	100	10.1	0.38
632	7.9	5.77	0.05	3273	108	10.23	0.4
674	8.7	5.88	0.05	3379	116	10.37	0.42
717	9.5	5.99	0.06	3486	125	10.51	0.44
762	10	6.1	0.06	3596	134	10.65	0.46
808	11	6.21	0.07	3710	144	10.78	0.49
856	12	6.32	0.07	3827	155	10.92	0.51
905	13	6.44	0.07	3947	165	11.06	0.54
955	14	6.55	0.08	4070	177	11.19	0.56
1008	15	6.66	0.09	4196	189	11.33	0.59
1062	17	6.78	0.09	4324	202	11.47	0.62
1118	18	6.89	0.1	4457	215	11.6	0.65
1176	19	7	0.1	4592	242	11.74	0.69
1235	21	7.12	0.11	4736	275	11.87	0.74
1296	22	7.23	0.12	4889	313	12	0.79
1358	24	7.35	0.12	4929	323	12.03	0.8

Tabulated data showing stress (P_x), stress uncertainty (σ_{P_x}), density (ρ) and density uncertainty (σ_ρ). All uncertainties are 1σ.